Effects of current on wind waves in strong winds

Naohisa Takagaki[1], *Naoya Suzuki*[2], *Yuliya Troitskaya*[3], *Chiaki Tanaka*[2], *Alexander Kandaurov*[3], *Maxim Vdovin*[3]

[1] (Corresponding Author) Department of Mechanical Engineering, University of Hyogo, Shosha 2167, Himeji Hyogo, 671-2280 Japan, *E-mail: takagaki@eng.u-hyogo.ac.jp*
Tel/Fax: +81-79-267-47834

[2] Faculty of Science and Engineering, Kindai University, 3-4-1, Kowakae Higashiosaka Osaka, 577-8502 Japan.

[3] Department of Geophysical Research, Institute of Applied Physics, the Russian Academy of Sciences, 46 Ul'yanov Street, Nizhny Novgorod, 603-950, Russia.

Keywords: wind waves, current, Doppler shift

Abstract

It is important to investigate the effects of current on wind waves, called the Doppler shift, both at normal and extreme high wind speeds. Three different types of wind-wave tanks along with a fan and pump are used to demonstrate wind waves and currents in laboratories at Kyoto University, Japan, Kindai University, Japan, and the Institute of Applied Physics, Russian Academy of Sciences, Russia. Profiles of the wind and current velocities and the water-level fluctuation are measured. The wave frequency, wavelength, and phase velocity of the significant waves are calculated, and the water velocities at the water surface and in the bulk of the water are also estimated by the current distribution. The study investigated 27 cases with carrying winds, waves, and currents, at wind speeds ranging from 7 to 67 m s^{-1}. ~~The results show that 27 different types of currents can be generated at wind speeds ranging from 7 to 67 m s^{-1}.~~ At normal wind speeds under 30 m s^{-1}, wave frequency, wavelength, and phase velocity depend on wind speed and fetch. The effect of the Doppler shift is confirmed at normal wind speeds, i.e., the significant waves are accelerated by the surface current. The phase velocity can be represented as the sum of the surface current and artificial phase velocity, which is estimated by the dispersion relation of the deep-water waves. At extreme high wind speeds, over 30 m s^{-1}, a similar Doppler shift is observed as under the conditions of normal wind speeds. This suggests

that the Doppler shift is an adequate model for representing the acceleration of wind waves by current, not only for the wind waves at normal wind speeds but also for those with intensive breaking at extreme high wind speeds. A weakly nonlinear model of surface waves at a shear flow is developed. It is shown that it describes well the dispersion properties of not only small-amplitude waves but also strongly nonlinear and even breaking waves, typical for extreme wind conditions (over 30 m s^{-1}).

1. Introduction

The oceans flow constantly, depending on the rotation of the Earth ~~earth's rotation~~, tides, ~~ground shape~~ topography, and wind shear. High-speed continuous ocean flows are called currents. Although the mean surface velocity of the ocean is approximately 0.1 m s^{-1}, ~~the maximum surface velocity for the currents is 1 m/s~~ the maximum current surface velocity is more than 1 m s^{-1} (e.g., Kawabe, 1988; Kelly et al., 2001). The interaction between the current and wind waves generated by ~~the~~ wind shear have been investigated in several studies. The acceleration effects of the current on wind waves, called the Doppler shift; ~~(well known as the Doppler shift),~~ the effects of the current on the momentum and heat transfer across the sea surface; ~~a sea surface,~~ and the modeling of waves and currents in the Gulf Stream have been the subject of experimental and numerical investigations (e.g., Dawe and Thompson, 2006; Kara et al., 2007; Fan et al., 2009; Shi and Bourassa, 2019). Thus, wind waves follow the dispersion relationship and Doppler shift effect at normal wind speeds. However, these studies were performed at normal wind speeds only, and few studies have been conducted at extreme high wind speeds, for which the threshold velocity is 30 – 35 m s^{-1}, representing the regime shift of the air-sea momentum, heat, and mass transport (Powell et al., 2003; Donelan et al., 2004; Takagaki et al., 2012, 2016; Troitskaya et al., 2012, 2020; Iwano et al., 2013; Krall and Jähne, 2014; Komori et al., 2018; Krall et al., 2019). At such extremely high wind speeds, the water surface is intensively broken by the strong wind shear, along with the foam layer, dispersed droplets, and entrained bubbles (e.g. Donelan et al., 2004; Troitskaya et al., 2012, 2017, 2018a, 2018b; Takagaki et al., 2012, 2016; Holthuijsen et al., 2012). It is unclear if the properties of wind waves and the surface foam layer at extremely high wind speeds are similar to those at normal wind speeds. Furthermore, in a hurricane, the local ocean flows may be unusually strong, change rapidly, and strongly affect wind waves. ~~At such extreme high wind speeds, owing to the intensive breaking by the strong wind shear, the local ocean flows might be strong. Furthermore, under a hurricane, the directions of the wind and ocean flows rapidly change; thus, the wind waves under a hurricane might~~

be strongly affected by complicated local ocean flows. However, the effects of the current on wind waves have not yet been clarified.

Therefore, the purpose of this study is to investigate the effects of the current on wind waves in strong winds through the application of three different types of wind-wave tanks, along with a pump.

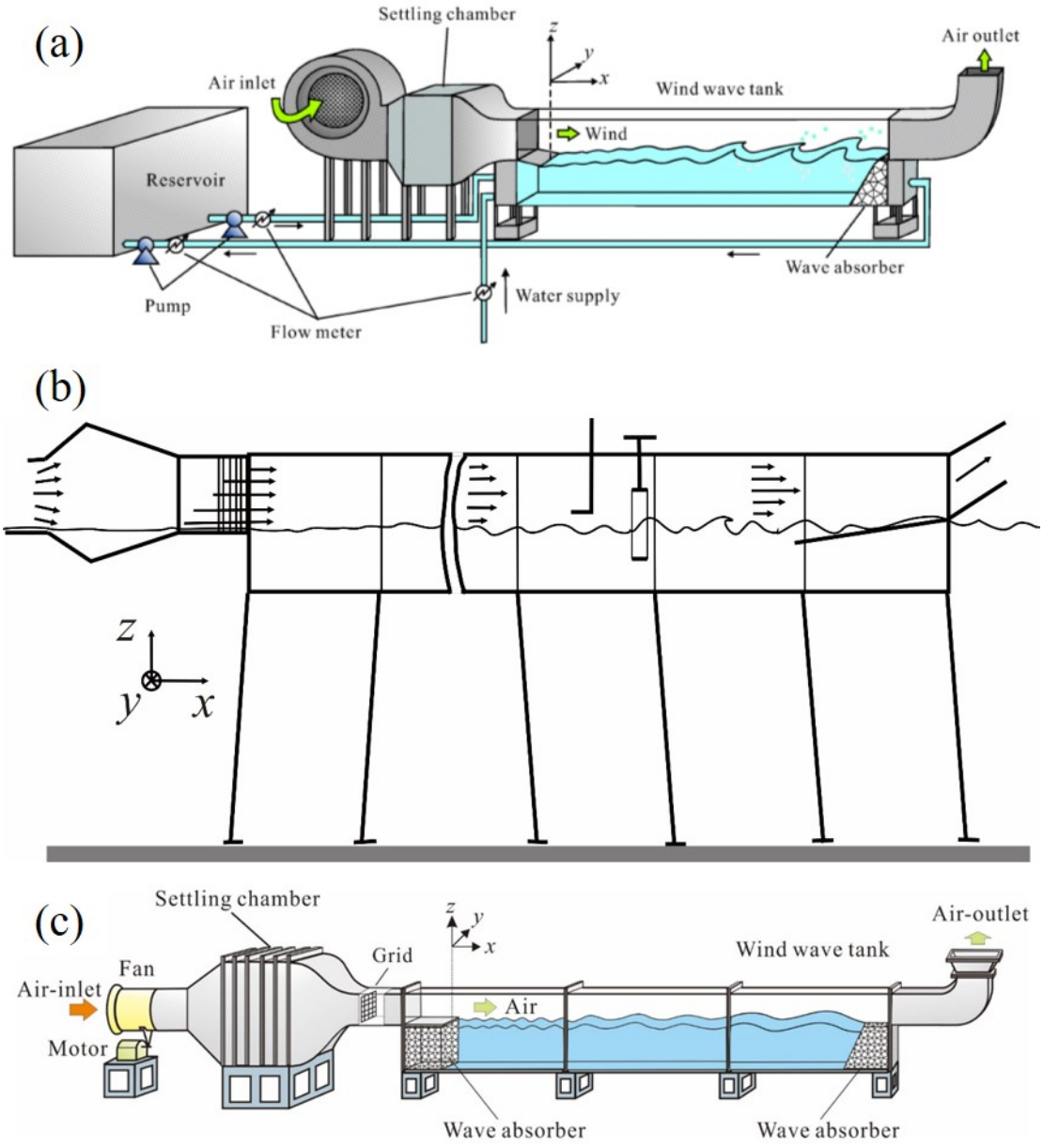

Figure 1. Schematics of wind-wave tanks. (a) High-speed wind-wave tank of Kyoto University. (b) Typhoon simulator of IAP RAS. (c) Wind-wave tank of Kindai University.

2. Experiment

2.1. Equipment and measurement methods

Wind-wave tanks at Kyoto University, Japan and the Institute of Applied Physics, Russian Academy of Sciences (IAP RAS) were used in the experiments (Figs. 1a, 1b). For the tank at Kyoto University, the glass test section was 15 m long, 0.8 m wide, and 1.6 m high. The water depth D was set at 0.8 m. For the tank at IAP RAS, the test section in the air side was 15 m long, 0.4 m wide, and 0.4 m high. The water depth D was set at 1.5 m. The wind was set to blow over the filtered tap water in these tanks, generating wind waves. The wind speeds ranged from 4.7 to 43 m s^{-1} and from 8.5 to 21 m s^{-1} in the tanks at Kyoto and IAP RAS, respectively. Measurements of the wind speeds, water-level fluctuation, and current were carried out 6.5 m downstream from the edge (x = 0 m) in both the Kyoto and IAP RAS tanks. Here, the x, y, and z coordinates are referred to as the streamwise, spanwise, and vertical directions, respectively, with the origin located at the center of the edge of the entrance plate. Additionally, the fetch (x) is defined as the distance between the origin and measurement point (x = 6.5 m).

In Kyoto, a laser Doppler anemometer (Dantec Dynamics LDA) and phase Doppler anemometer (Dantec Dynamics PDA) were used to measure the wind velocity fluctuation. A high-power multi-line argon-ion (Ar^+) laser (Lexel model 95-7; laser wavelengths of 488.0 and 514.5 nm) with a power of 3 W was used. The Ar^+ laser beam was shot through the sidewall (glass) of the tank. Scattered particles with a diameter of approximately 1 μm were produced by a fog generator (Dantec Dynamics F2010 Plus) and were fed into the air flow over the waves (see Takagaki et al. (2012) and Komori et al. (2018) for details). The wind speed values (U_{10}) at a height of 10 m heigh above the ocean and the friction velocity (u^*) were estimated by the eddy correlation method, by which the mean velocity (U) and the Reynolds stress ($-uv$) in air were measured. The u^* was estimated by an eddy correlation method as $u^* = (-\langle uv \rangle)^{1/2}$, because the shear stress at the interface (τ) was defined by $\tau = \rho u^{*2} = \rho C_D U_{10}^2$. The value of $(-\langle uv \rangle)^{1/2}$ was estimated by extrapolating the measured values of the Reynolds stress to the mean surface of z = 0 m. The U_{10} was estimated by the log-law: $U_{10} - U_{min} = u^*/\kappa \ln(z_{10}/z_{min})$, where U_{min} is the air velocity nearest the water surface (z_{min}) and z_{10} is 10 m. Moreover, the drag coefficient C_D was estimated by $C_D = (u^*/U_{10})^2$.

Water level fluctuations were measured using resistance-type wave gauges (Kenek CHT4-HR60BNC) in Kyoto. The resistance wire was placed into the water, and the electrical resistance at the instantaneous water level was recorded at 500 Hz for 600 s using a digital recorder (Sony EX-UT10). The energy of the wind waves (E) was

estimated by integrating the spectrum of the water-level fluctuations over the frequency (f). The values of the wavelength (L_S) and phase velocity (C_S) were estimated using the ~~cospectra~~ corss-spectrum method (e.g., Takagaki et al., 2017) (see the detail in Appendix). The current was measured using the same LDA system.

In IAP RAS, a hot-wire anemometer (E+E Electrinik EE75) was used to measure the representative mean wind velocity at x = 0.5 m and z = 0.2 m. The three wind velocities (U_{10}, u^*, U_∞) at x = 6.5 m were taken from Troitskaya et al. (2012) by a Pitot tube. Here, U_∞ is the freestream wind speed. The u^* was estimated by a profile method considering the profiles in the constant flux layer and the wake region:

$$U_\infty - U(z) = u^*\left(-\frac{1}{\kappa}ln(z/\delta) + \alpha\right);\ z/\delta < 0.15, \quad (1)$$

$$U_\infty - U(z) = \beta u^*(1 - z/\delta)^2;\ z/\delta > 0.15, \quad (2)$$

respectively. Here, δ is the boundary layer thickness, and α and β are the constant values that depend on flow fields and are calibrated at low wind speeds without the dispersed droplets. At extremely high wind speeds, measuring the profile in the constant flux layer (Eq. 1) is difficult because of the large waves; thus, using β measured at low wind speeds, u^* is estimated by Eq. (2). The value of U_{10} is estimated by Eq. (1) at z_{10} = 10 m with measured α at normal wind speeds. The value of C_D is estimated by $C_D = (u^*/U_{10})^2$. Although the measurement methods for u^*, U_{10}, and C_D in IAP RAS and Kyoto are different, the values approximately correspond to each other (see Troitskaya et al. (2012) and Takagaki et al. (2012)).

The water-level fluctuations were measured using three handmade capacitive-type wave gauges in IAP RAS. Three wires formed a triangle with 25 mm on a side (x-directional distance between wires Δx is 21.7 mm). The wires were placed in the water, and the output voltages at the instantaneous water level were recorded at 200 Hz for 5400 s using a digital recorder through an AD converter (L-Card E14-140). The values (E, f_m, H_S, T_S, C_S, and L_S) were estimated by the same mannar as in Kyoto tank. The current was measured through acoustic Doppler velocimetry (Nortec AS) at x = 6.5 m and z = −10, −30, −50, −100, −150, −220, and −380 mm (see Troitskaya et al. (2012) for details).

2.2. Artificial current experiments at Kindai University

Additional experiments were performed using a wind-wave tank at Kindai University with a glass test section 6.5 m long, 0.3 m wide, and 0.8 m high (Fig. 1c) (e.g. Takagaki et al., 2020). The water depth D was set at 0.49 m. A Pitot tube (Okano Works,

LK-0) and differential manometers (Delta Ohm HD402T) were used to measure the mean wind velocity. The values of u^*, U_{10}, and C_D (Cases 21-27) were estimated using U_∞ by the empirical curve by Iwano et al. (2013), which was proposed by the eddy correlation method used in Kyoto (see section 2.1).

The water level fluctuations were measured using resistance-type wave gauges (Kenek CHT4-HR60BNC). To measure L_S and C_S, another wave gauge was fixed downstream at Δx = 0.02 m, where Δx is the interval between the two wave gauges. The values (E, f_m, H_S, T_S, C_S, and L_S) were estimated by the same mannar as in Kyoto tank. The current was then measured through electromagnetic velocimetry (Kenek LP3100) with a probe (Kenek LPT-200-09PS) at x = 4.0 m. The probe sensing station was 22 mm long with a diameter of 9 mm. The measurements were performed at z = −15 to −315 mm at 30 mm intervals. The sampling frequency was 8 Hz, and the sampling time was 180 s.

3. Results and discussion

3.1. Waves and current

Figure 2 shows the vertical distributions of the streamwise water velocity. The water velocities in the three different wind-wave tanks at Kyoto University, Kindai University, and IAP RAS are separately shown in each subfigure. In Fig. 2a, the bulk velocity of water U_{BULK} shows negative values (U_{BULK} = −0.16 to −0.01 m s^{-1}) at Kyoto University, which is generated as the counterflow against the Stokes drift at the wavy water surface. In Fig. 2b, the bulk velocity of water demonstrates positive values (U_{BULK} = 0.019 to 0.044 m/s) at IAP RAS, because the wind-wave flume is submerged; thus, the Stokes drift on the wavy water surface does not provide the counterflow for the bulk water, unlike in the closed tank at Kyoto University. ~~This is because the wind-wave tank at IAP RAS is an open tank; thus, the Stokes drift on the wavy water surface does not provide the counterflow for the bulk water, unlike in the closed tank at Kyoto University.~~ From Fig. 2c, it is clear that the bulk velocities of the water vary in each case at Kindai University with the use of the pump. Furthermore, the water bulk velocities change from negative to positive (U_{BULK} = −0.13 to −0.17 m s^{-1}). The bulk velocities of water were defined as the mean velocity with z = −0.4 to −0.25 m (see dotted lines in Fig. 2), and the velocities are listed in Table 1. Experiments were performed under 27 different conditions, with the bulk velocity of water provided in the three different wind-wave tanks. The surface velocities of water, U_{SURF}, also varied in the three tanks with respect to wind speed (see Fig. 2). The U_{SURF} values were estimated by the linear extrapolation lines (dashed lines) as the water velocity at the surface (z = 0 m) shown in Fig. 2, and the velocities are listed in Table 1.

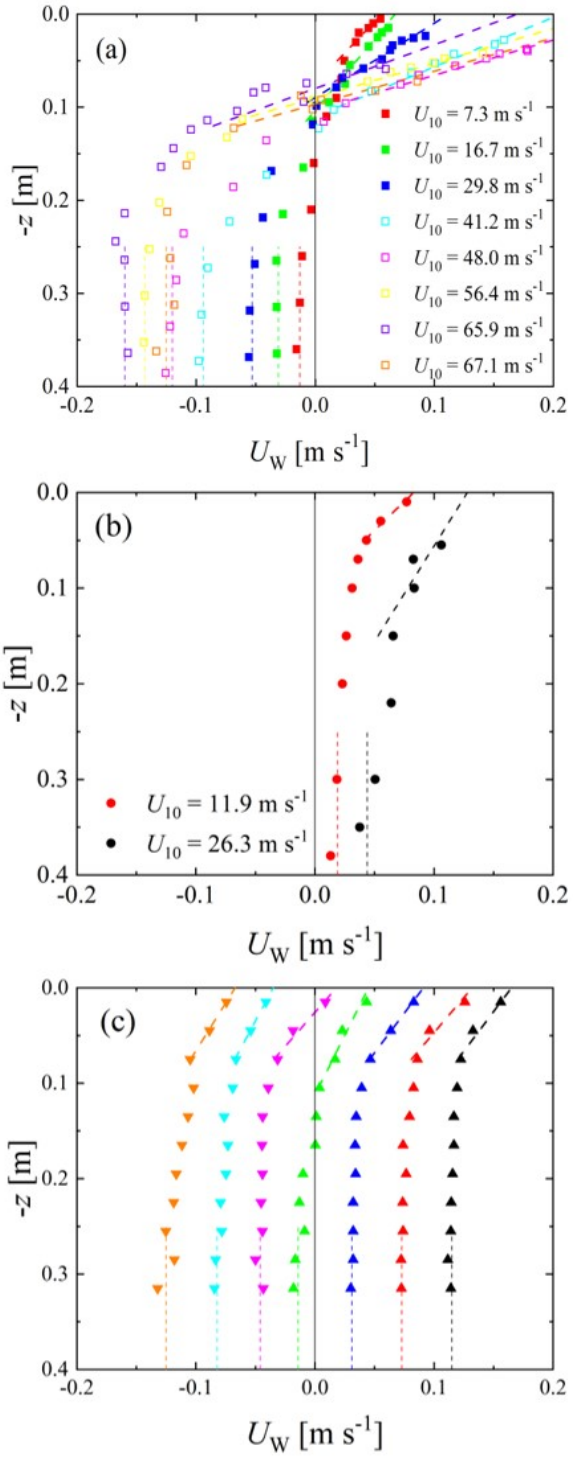

Figure 2. Vertical distributions of water-flow velocity; (a) Kyoto University, (b) IAP RAS, and (c) Kindai University. In (c), plots indicate cases 21–27 starting from right. Dotted and dashed lines indicate the lines used to estimate U_{BULK} and U_{SURF}, respectively. Open symbols show the high-wind-speed cases.

TABLE 1. Wind and wind-wave properties. F: fetch; N_{PUMP}: pump inverter frequency; U_∞: freestream wind speed; u^*: friction velocity of air; U_{10}: wind speed at 10 m above the sea surface; U_{SURF}: surface flow velocity of water; U_{BULK}: bulk flow velocity of water; C_D: drag coefficient; H_S: significant wave height; T_S: significant wave period; E: wave energy; f_m: significant frequency; C_S: phase velocity; L_S: significant wave length; $C_{S\text{-theor-l}}$: phase velocity predicted by theoretical linear model; $C_{S\text{-theor-nl}}$: phase velocity predicted by theoretical nonlinear model. The values of u^*, U_{10}, and C_D in Kindai were estimated using the empirical curves by Iwano et al. (2013) from U_∞. Superscripts † and †† indicate the artificial following and opposing flows, respectively.

Case	Facility	F [m]	N_{pump} [Hz]	U_∞ [m s^{-1}]	u^* [m s^{-1}]	U_{10} [m s^{-1}]	U_{SURF} [m s^{-1}]	U_{BULK} [m s^{-1}]	C_D [×10^{-3}]	H_s [m]	T_s [m]	$E^{0.5}$ [m]	f_m [Hz]	C_s [m s^{-1}]	L_s [m]	$C_{s\text{-theor-l}}$ [m s^{-1}]	$C_{s\text{-theor-nl}}$ [m s^{-1}]
1	Kyoto	6.5	-	4.7	0.24	7.3	0.056	-0.01	1.1	0.0035	0.15	0.00092	6.63	0.40	0.06	0.369	0.374
2	Kyoto	6.5	-	7.2	0.43	11.5	-	-	1.4	0.0131	0.25	0.00353	3.95	0.59	0.16	-	-
3	Kyoto	6.5	-	10.3	0.67	16.7	0.067	-0.031	1.6	0.0231	0.32	0.00624	3.03	0.69	0.23	0.658	0.690
4	Kyoto	6.5	-	12.6	0.89	21.5	-	-	1.7	0.0357	0.39	0.00968	2.59	0.92	0.38	-	-
5	Kyoto	6.5	-	16.3	1.49	29.8	0.112	-0.053	2.5	0.0584	0.50	0.01570	2.01	1.09	0.52	0.972	1.044
6	Kyoto	6.5	-	18.8	1.70	33.6	-	-	2.5	0.0626	0.52	0.01691	1.89	1.18	0.60	-	-
7	Kyoto	6.5	-	22.2	2.08	41.2	0.206	-0.094	2.6	0.0631	0.53	0.01735	1.86	1.35	0.74	1.188	1.258
8	Kyoto	6.5	-	24.8	-	-	-	-	-	0.0668	0.55	0.01866	1.76	1.41	0.79	-	-
9	Kyoto	6.5	-	28.5	2.36	48.0	0.273	-0.120	2.4	0.0727	0.58	0.02058	1.68	1.54	0.93	1.325	1.424
10	Kyoto	6.5	-	31.1	-	-	-	-	-	0.0807	0.62	0.02309	1.58	1.60	1.07	-	-
11	Kyoto	6.5	-	34.8	2.69	56.4	0.241	-0.143	2.3	0.0944	0.68	0.02715	1.44	1.64	1.10	1.379	1.550
12	Kyoto	6.5	-	37.1	2.89	57.7	-	-	2.5	0.1043	0.73	0.03027	1.37	1.76	1.31	-	-
13	Kyoto	6.5	-	39.6	3.38	65.9	0.170	-0.160	2.6	0.1214	0.80	0.03553	1.20	1.84	1.51	1.531	1.694
14	Kyoto	6.5	-	43.3	3.31	67.1	0.272	-0.125	2.4	0.1609	0.93	0.04766	1.08	2.01	1.92	1.743	2.149
15	IAP RAS	6.5	-	8.5	0.40	11.9	0.083	0.019	1.1	0.0214	0.31	0.0056	3.14	0.78	0.25	0.690	0.715
16	IAP RAS	6.5	-	11.0	0.60	16.7	-	-	1.3	0.0305	0.36	0.0081	2.84	0.89	0.32	-	-
17	IAP RAS	6.5	-	13.5	0.90	21.9	-	-	1.7	0.0455	0.43	0.0121	2.41	1.07	0.45	-	-
18	IAP RAS	6.5	-	16.3	1.15	26.3	0.128	0.044	1.9	0.0790	0.50	0.0161	1.95	1.27	0.65	1.111	1.190
19	IAP RAS	6.5	-	18.9	1.50	32.5	-	-	2.1	0.0690	0.54	0.0246	1.85	1.37	0.74	-	-
20	IAP RAS	6.5	-	21.2	1.70	36.9	-	-	2.1	0.0847	0.60	0.0305	1.61	1.61	1.00	-	-
21	Kindai	4.0	15†	5.8	0.28	7.9	0.165	0.115	1.2	0.0044	0.14	0.0012	6.92	0.43	0.06	0.484	0.492
22	Kindai	4.0	10†	5.8	0.28	7.9	0.132	0.073	1.2	0.0050	0.16	0.0014	6.10	0.43	0.07	0.501	0.510
23	Kindai	4.0	5†	5.8	0.28	7.9	0.091	0.031	1.2	0.0049	0.16	0.0014	6.16	0.38	0.06	0.410	0.420
24	Kindai	4.0	0	5.8	0.28	7.9	0.045	-0.014	1.2	0.0054	0.19	0.0014	5.47	0.38	0.07	0.382	0.393
25	Kindai	4.0	5††	5.8	0.28	7.9	0.018	-0.046	1.2	0.0076	0.23	0.0021	4.25	0.36	0.08	0.384	0.400
26	Kindai	4.0	10††	5.8	0.28	7.9	-0.035	-0.082	1.2	0.0098	0.27	0.0027	3.64	0.35	0.10	0.355	0.375
27	Kindai	4.0	15††	5.8	0.28	7.9	-0.067	-0.125	1.2	0.0125	0.34	0.0035	2.94	0.38	0.13	0.381	0.402

Figure 3 shows the wind-velocity dependency of the wave frequency f_m, wavelength L_S, phase velocity C_S, surface velocity of water U_{SURF}, and bulk velocity of water U_{BULK}. From Figs. 3a–3c, it is clear that both the Kyoto and IAP RAS data demonstrate that the wind waves develop with wind shear. Although f_m in both cases correspond to each other, L_S and C_S in IAP RAS are different from those in Kyoto. The disagreement might be caused by the difference in the wind-wave development or Doppler effect; this is discussed below. From Figs. 3d and 3e, U_{SURF} and U_{BULK} increase

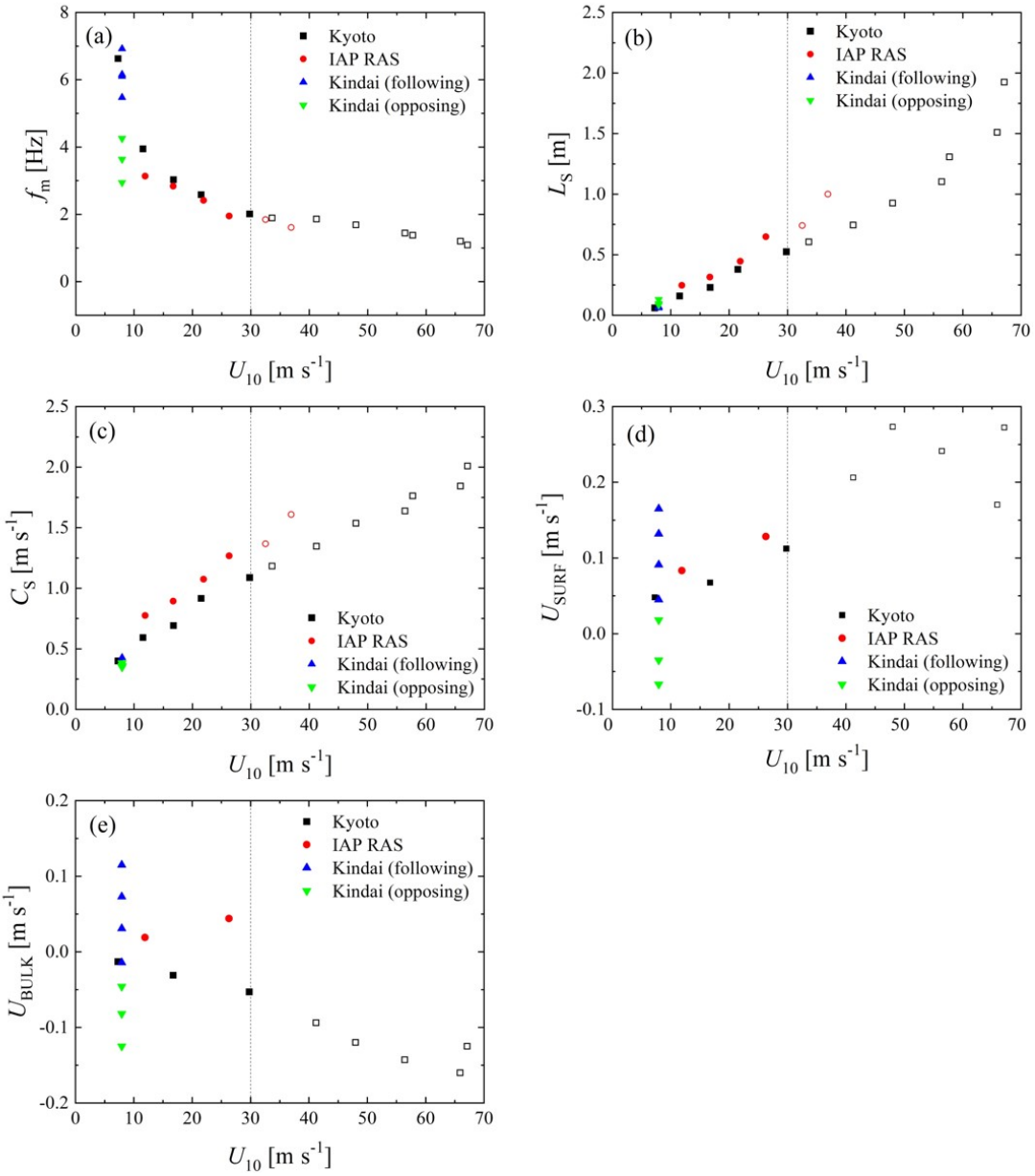

Figure 3. Relationships between U_{10} and (a) significant frequency f_m, (b) significant wave length L_S, (c) phase velocity C_S, (d) surface velocity of water U_{SURF}, and (e) bulk velocity of water U_{BULK}. Open symbols show the high-wind-speed cases.

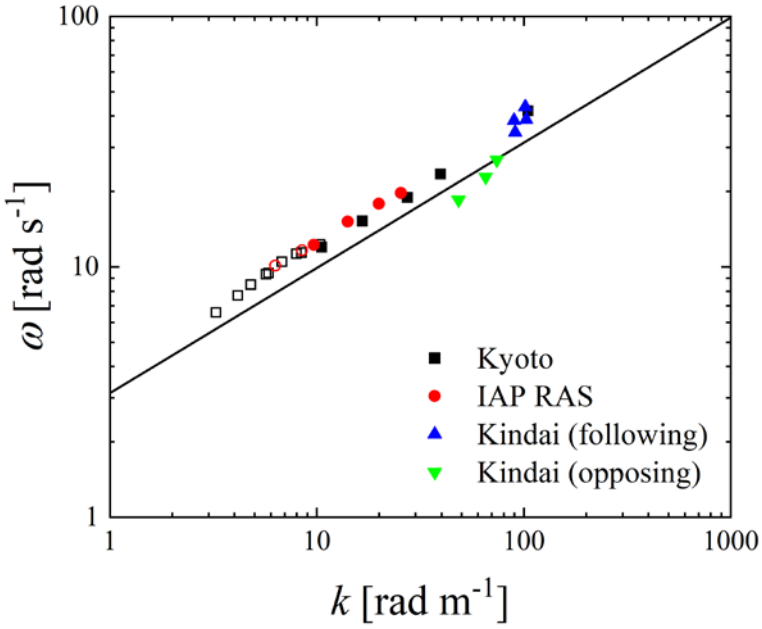

Figure 4. Dispersion relation between angular frequency ω and wave number k. Open symbols show the high-wind-speed cases. Curve shows the dispersion relation of the deep-water waves ($\omega^2 = gk$).

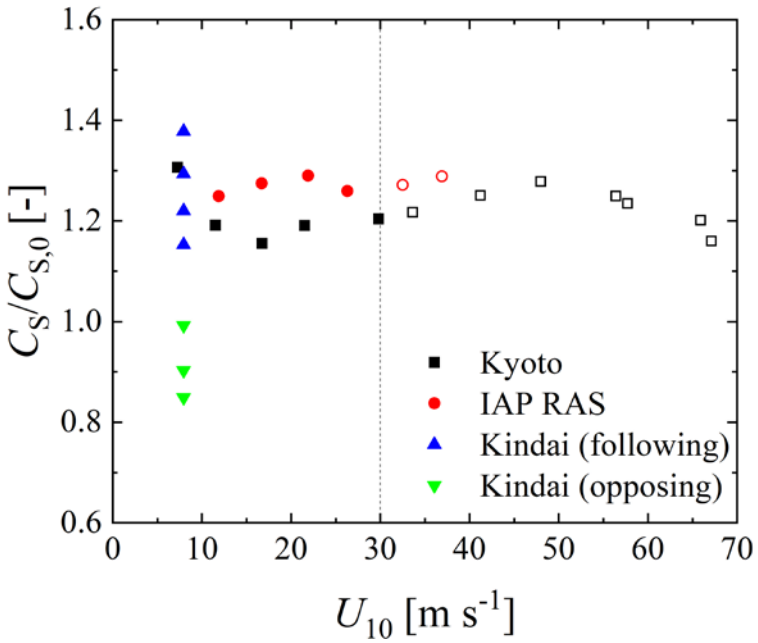

Figure 5. Relationship between the freestream wind speed and phase velocity C_S. The C_S is normalized by phase velocity $C_{S,0}$ without the Doppler effect, estimated by the dispersion relation of the deep-water waves ($C_{S,0} = (gL_S/2\pi)^{1/2}$). Open symbols show the high-wind-speed cases.

with an increase in U_{10} in IAP RAS. However, in Kyoto, U_{SURF} increases, but U_{BULK} decreases with an increase in U_{10}. Moreover, U_{SURF} in IAP RAS corresponds to U_{SURF} in Kyoto. This is because the Stokes drift generated by the wind waves, rather than the current, is significant. For the Kindai data, although f_m, U_{SURF}, and U_{BULK} vary, L_S and C_S are concentrated at single points at L_S = 0.1 m and C_S = 0.4 m s^{-1}, respectively. This shows that the intensity and direction of the current do not significantly affect L_S and C_S but do affect f_m and U_{SURF}. Thus, this implies that the present artificial current changes the water flow dramatically but does not affect the development of the wind waves.

Figure 4 shows the dispersion relation and demonstrates that the Kindai data points depend on the variation in the water velocity of the artificial current. The plots for the Kyoto University and IAP RAS cases at normal wind speeds (solid symbols) are concentrated above the solid curve, showing the dispersion relation of the deep-water waves ($\omega^2 = gk$). Meanwhile, the plots for extreme high wind speeds (open symbols) are also concentrated above the solid curve. This implies that the wind waves, along with the intensive breaking at extreme high wind speeds, are dependent on the Doppler shift. To investigate the phase velocity trend, Fig. 5 shows the ratio of the measured phase velocity C_S to the phase velocity $C_{S,0}$ estimated by the dispersion relation of the deep-water waves ($C_{S,0} = (gL_S/2\pi)^{1/2}$) against the wind velocity. From the figure, the ratios at the normal wind speeds assume a constant value (~1.21 in Kyoto or ~1.27 in IAP RAS). Moreover, the ratios at the extreme high wind speeds take similar values of 1.23 and 1.28 for Kyoto or IAP RAS, respectively. This implies that the phase velocities at extreme high wind speeds are accelerated by the current just as those at normal wind speeds. However, the Kindai values are scattered and increase in the following cases and decrease in the opposing cases. It is clear that the artificial current accelerates (or decelerates) the phase velocity.

To interpret the relationship among the measured phase velocity C_S, first phase velocity $C_{S,0}$ estimated by the dispersion relation, and water velocity, two types of phase velocity were evaluated: the sum of $C_{S,0}$ and surface velocity of water U_{SURF} and the sum of $C_{S,0}$ and bulk velocity of water U_{BULK}. Figure 6 shows the relationship between C_S and (a) $C_{S,0} + U_{SURF}$, and (b) $C_{S,0} + U_{BULK}$. In Fig. 6a, we can see that the Doppler shift is confirmed at the normal wind speeds, i.e., the significant waves are accelerated by the surface flow, and the real phase velocity can be represented as the sum of the velocity of the surface flow and the virtual phase velocity, which is estimated by the dispersion relation of the deep-water waves. At extreme high wind speeds over 30 m s^{-1}, a similar Doppler shift is observed as under the conditions of normal wind speeds, as seen in Fig. 6a. Meanwhile, in Fig. 6b, although C_S corresponds to $C_{S,0} + U_{BULK}$ at low phase

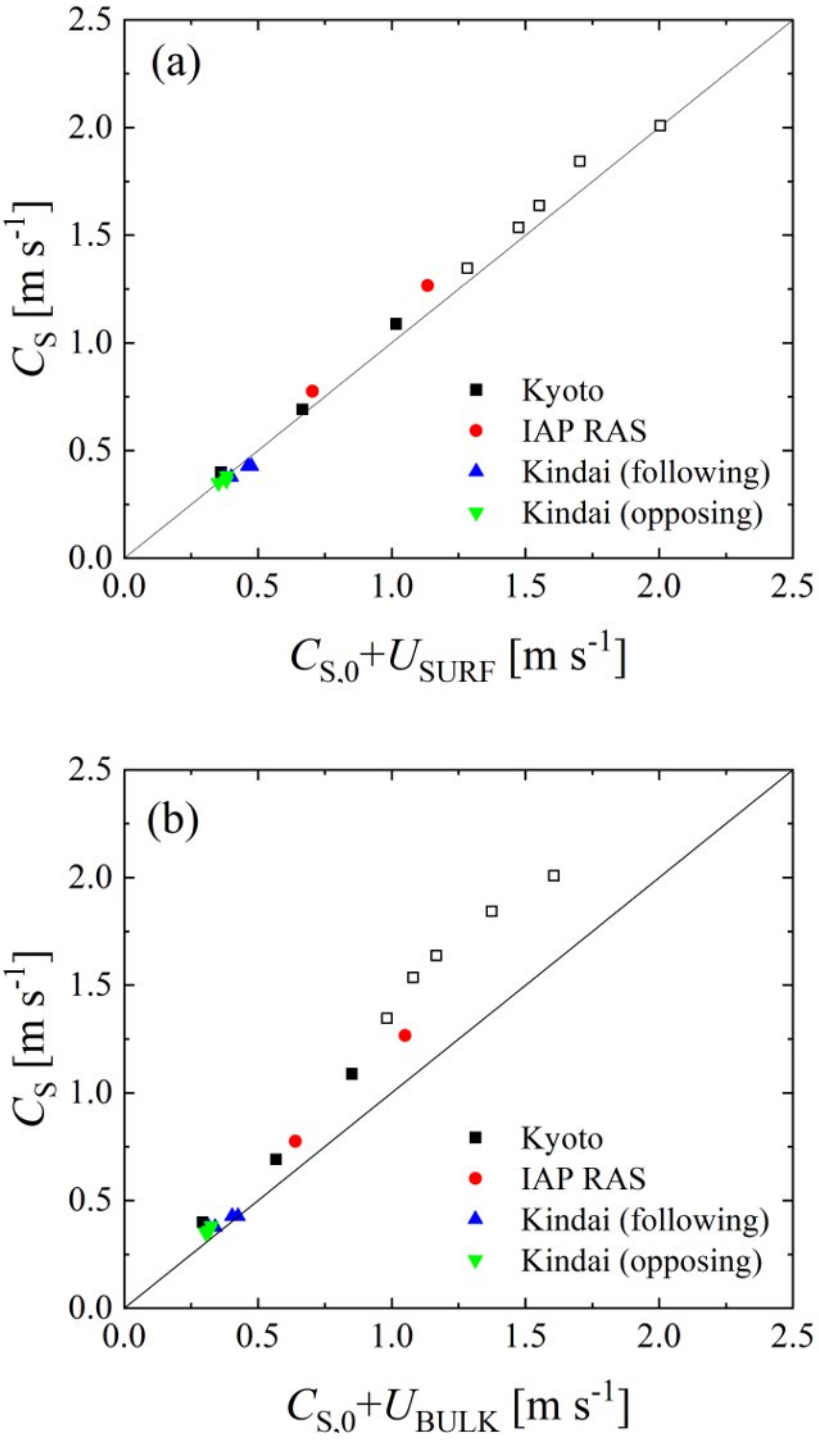

Figure 6. Relationship between phase velocity C_S and (a) sum of $C_{S,0}$ and surface velocity of water U_{SURF}, and (b) sum of $C_{S,0}$ and bulk velocity of water U_{BULK}. Open symbols show the high-wind-speed cases.

264 velocities, C_S assumes values larger than $C_{S,0} + U_{BULK}$ at high phase velocities. This
265 suggests that the Doppler shift is an adequate model for representing the acceleration of
266 the wind waves by the current, not only for the wind waves at normal wind speeds but
267 also for those with intensive breaking at extreme high wind speeds. Moreover, the
268 Doppler shift of wind waves occurs due to a very thin surface flow, as the correlation
269 between C_S and $C_{S,0} + U_{SURF}$ is higher than the correlation between C_S and $C_{S,0} + U_{BULK}$.
270
271 **3.2. The theoretical model of waves at the shear flow**
272 The parameters of the observed Doppler shift can be explained more precisely
273 within the theoretical model of the capillary-gravity waves at the surface of the water
274 flows with the velocity profiles prescribed by the experimental data, which are plotted in
275 Fig. 2a–c. Because the dominant wind wave propagates along the wave and water flows,
276 we will consider the 2D-wave model in the 2D flow. This flow is described by the system
277 of 2D Euler equations:

278
$$\frac{\partial u}{\partial t} + u\frac{\partial u}{\partial x} + w\frac{\partial u}{\partial z} + \frac{1}{\rho}\frac{\partial p}{\partial x} = 0, \qquad (3)$$

279
$$\frac{\partial w}{\partial t} + u\frac{\partial w}{\partial x} + w\frac{\partial w}{\partial z} + \frac{1}{\rho}\frac{\partial p}{\partial z} = -g,$$

280 and the condition of non-compressibility:

281
$$\frac{\partial u}{\partial x} + \frac{\partial w}{\partial z} = 0, \qquad (4)$$

282 with the kinematical

283
$$\frac{\partial \eta}{\partial t} + u\frac{\partial \eta}{\partial x} = w\big|_{z=\eta(x,t)} \qquad (5)$$

284 and dynamical boundary conditions

285
$$p\big|_{z=\eta(x,t)} = 0 \qquad (6)$$

286 at the water surface. Here, u and w are the horizontal and vertical velocity components, p
287 is the water pressure, x and z are the horizontal and upward vertical coordinates, g is the
288 gravity acceleration, and ρ is the water density. The boundary condition at the bottom of
289 the channel is $w\big|_{z=-D} = 0$. It should be noted that the water depth in almost all the
290 experimental runs exceeded half of the wavelength of the dominant waves (see Table 1).
291 In this case, the deep-water approximation is applicable for describing the surface waves,

and the boundary condition of the wave field vanishing with the distance from the water surface can also be used.

Because the fluid motion under consideration is 2D, the stream function can be introduced as follows:

$$u = \frac{\partial \psi}{\partial z}; w = -\frac{\partial \psi}{\partial x}. \tag{7}$$

To derive the linear dispersion relation for the surface waves at the plane shear flow with the horizontal velocity profile $U_w(z)$, we consider the solution to Eqs. ~~(1, 2)~~ (3, 4) in terms of the stream function as the sum of the undisturbed state with steady shear flow and small-amplitude disturbances. Then, the stream function ψ and pressure p are as follows:

$$\psi(x,z,t) = \int^{z} U_w(z_1)\,dz_1 + \varepsilon\psi_1(x,z,t); \tag{8}$$

$$p(x,z,t) = -\rho g z + \varepsilon p_1(x,z,t), \tag{9}$$

where $\varepsilon << 1$, and the water elevation value is also the order of ε, namely $\varepsilon\eta_1(x, t)$.

In the linear approximation in ε, the system of Eqs. ~~(1, 2)~~ (3, 4) and the boundary conditions of Eqs. ~~(3, 4)~~ (5, 6) take the form:

$$\left(\frac{\partial}{\partial t} + \frac{U_w(z)\partial}{\partial x}\right)\left(\frac{\partial^2 \psi_1}{\partial x^2} + \frac{\partial^2 \psi_1}{\partial z^2}\right) - \frac{\partial \psi_1}{\partial x}\frac{d^2 U_w(z)}{dz^2} = 0,$$

$$\frac{\partial \eta_1}{\partial t} + U_w(0)\frac{\partial \eta_1}{\partial x} = -\left.\frac{\partial \psi_1}{\partial x}\right|_{z=0}, \tag{10}$$

$$\left.\frac{\partial p_1}{\partial x}\right|_{z=0} - \rho g \frac{\partial \eta_1}{\partial x} = 0,$$

$$\left.\psi_1\right|_{z=-D} = 0.$$

Excluding p_1 with use of the first equation of the system in Eq. ~~(1)~~ (3) and eliminating η_1 yields one boundary condition at the water surface for ψ_1:

$$\left[\left(\frac{\partial}{\partial t} + \frac{U_w(0)\partial}{\partial x}\right)^2 \frac{\partial \psi_1}{\partial z} - \left(\frac{\partial}{\partial t} + U_w(0)\frac{\partial}{\partial x}\right)\frac{\partial \psi_1}{\partial x}\frac{dU_w}{dz} - g\frac{\partial^2 \psi_1}{\partial x^2}\right]_{z=0} = 0. \tag{11}$$

For the harmonic wave disturbance, where

$$\psi_1(x,z,t) = \Psi(t)\exp(-i(\omega t - kt)), \tag{12}$$

substituting into Eqs. ~~(8, 9)~~ (10, 11) yields the Rayleigh equation for the complex amplitude of the stream function disturbance:

$$(\omega - U_w(z)k)\left(\frac{d^2\Psi_1}{dz^2} - k^2\Psi_1\right) + \frac{d^2 U_w(z)}{dz^2}k^2\Psi_1 = 0, \tag{13}$$

with the following boundary condition:

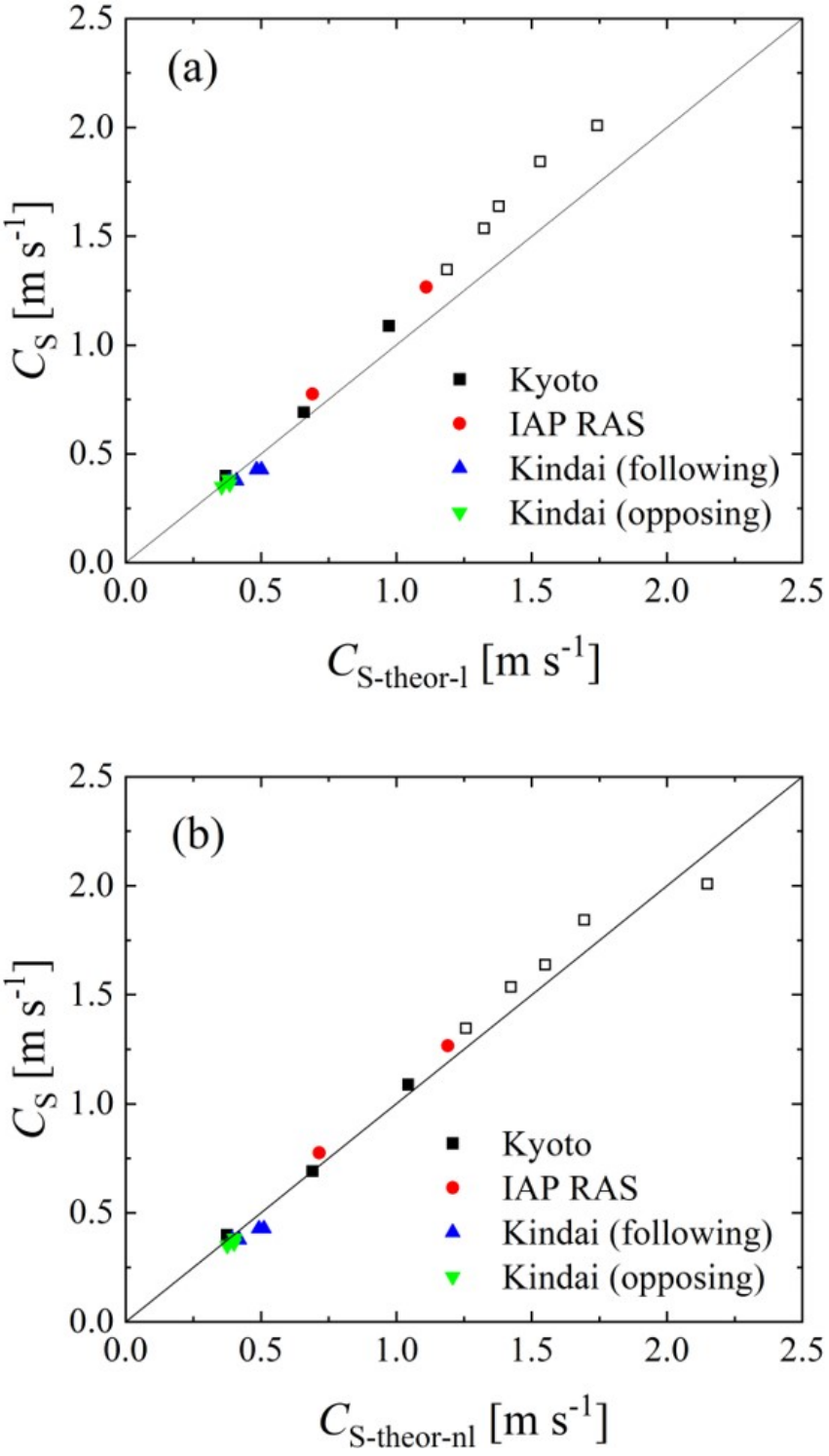

Figure 7. The measured phase velocity C_S versus theoretical prediction: (a) linear model, and (b) nonlinear model.

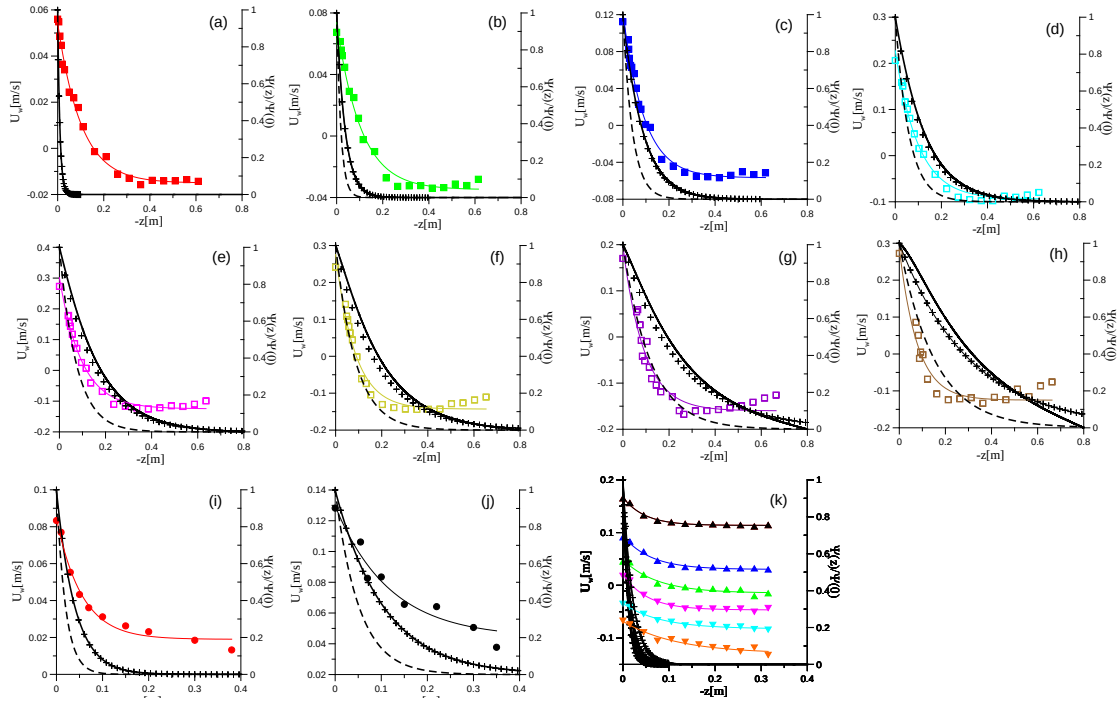

Figure 8. Vertical velocity profiles (points), their fitting (thin color line), the eigenfunction of the Eq. (8) with the boundary conditions Eq. (9) (black solid curve), the function e^{kz} (crosses), the function e^{2kz} (dashed line). The panels (a)-(j) corresponds to the experiments No. 1, 3, 5, 7, 9, 11, 13-15, 18 respectively, the panel (k) corresponds to the experiments No. 21-27.

$$(\omega - U_w(0)k)^2 \frac{d\Psi_1(0)}{dz} + (\omega - U_w(0)k)k\Psi_1(0)\frac{dU_w(0)}{dz} - k^2 g\Psi_1(0) = 0, \quad (14)$$

$$\Psi_1\big|_{z\to-\infty} \to 0.$$

Numerically solving the boundary layer problem for Eq. ~~(11)~~ (13) with the boundary conditions in Eq. ~~(12)~~ (14) enables one to obtain the dispersion relation $\omega(k)$ for the surface waves at the inhomogeneous shear flow. Note that because the phase velocity of the waves significantly exceeded the flow velocity in all experiments (cf. Figs. 2 and 3), the Rayleigh equation did not have a singularity, and the calculated frequency and phase velocity of the wave were real values, i.e., the current was neutral stable.

The wave phase velocities $C_{\text{S-theor-l}} = \omega(k)/k$ were calculated for the parameters of those experiments that contained complete information about the course and characteristics of the waves, namely 1, 3, 5, 7, 9, 11, 13–15, 18, and 21–27 from Table 1. The results are presented in Fig. 7a as the measured phase velocity Cs versus calculated phase velocity $C_{\text{S-theor-l}}$. One can see that the model corresponds to the data substantially

better than does the model of linear potential waves at the homogeneous current U_{BULK} (compare Fig. 6b). Considering the structure of the wave disturbances of the stream function, $\Psi_1(z)$, which was found as the eigenfunction of the boundary problem of Eqs. (11, 12). The profiles of $\Psi_1(z)$ are presented in Fig. 8. One can see that in all cases the functions $\Psi_1(z)$ are close to e^{kz} at the background of the mean velocity profiles. Moreover, for experiments No. 1, 3, 5, 15, and 21–27 (see Fig. 8a, 8b, 8c, 8i, and 8k), the wave field is concentrated near the surface at a distance less than the scale of the change in the mean flow, where the flow velocity is approximately equal to U_{SURF}. This explains the good correlation in these cases of the observed phase velocity with the phase velocity of waves at the homogeneous current U_{SURF} presented in Fig. 6a. At the same time, for experiments No. 7, 9, 5, 11, 13, 14, and 18 (see Figs. 8d–8h, and 8j), the scale of the variability of the flow is significantly smaller than the scale of the wave field. Under these conditions, a significant difference between the phase velocity of the waves and that given by the linear dispersion relation can be due to the influence of nonlinearity.

To estimate the nonlinear addition to the wave phase velocity, we used the results of the weakly nonlinear theory of surface waves for the current with a constant shear. Of course, the flow in the experiments of the present work does not have a constant shift, and this was considered when obtaining the linear dispersion relation. However, it should be taken into account that the contributions of the n-th harmonic to the nonlinear dispersion relation are determined by wave fields in the n-power, which have a scale that is n time smaller than the first harmonic. Additionally, the model of constant shear of the mean current velocity is already approximately applicable for the 2nd harmonic (see Fig. 8).

We use the nonlinear dispersion relation for waves in the current with a constant shift in the deep-water approximation, which was obtained by Simmen and Saffman (1985):

$$(\omega - U_w(0)k)^2 \frac{d\Psi_1(0)}{dz} + (\omega - U_w(0)k)k\Psi_1(0)\frac{dU_w(0)}{dz} - k^2 g\Psi_1(0) = \gamma(ka)^2,$$

$$\gamma = \frac{(\omega_0 - U_w(0)k)^2}{2k}\left(1 - \frac{1}{2}\Omega^2 + \left(1 + 2\Omega + \frac{1}{2}\Omega^2\right)^2\right), \quad (15)$$

$$\Omega = \frac{1}{(\omega_0 - U_w(0)k)}\frac{dU_w(0)}{dz},$$

Here, ω_0 is the solution of the linear dispersion equation. Eq. ~~(13)~~ (15) is rewritten in the notation of this work and formulated in a reference frame in which the surface of the water has the velocity $U_w(0)$. Note that the linear part of Eq. ~~(13)~~ (15) coincides with Eq. ~~(12)~~ (14). The results of solving Eq. ~~(13)~~ (15) are presented in Fig. 7b similarly to Fig. 7a as the measured phase velocity C_S versus calculated phase velocity $C_{S\text{-theor-nl}} = \omega(k)/k$,

where one can see their good agreement with each other. Thus, the wave frequency shift can be explained by two factors, including the Doppler shift at the mean flow and the nonlinear frequency shift, while, the latter can also be interpreted in its physical nature as the wave frequency shift in the presence of its orbital velocities.

Recent studies have indicated a regime shift in the momentum, heat, and mass transfer across an intensive broken wave surface along with the amount of dispersed droplets and entrained bubbles at extreme high wind speeds over 30 m s^{-1} (e.g., Powell et al., 2003; Donelan et al., 2004; Takagaki et al., 2012, 2016; Troitskaya et al., 2012; Iwano et al., 2013; Krall and Jähne, 2014; Komori et al., 2018; Krall et al., 2019). Thus, there is the possibility of a similar regime shift in the Doppler shift of wind waves by the current at extreme high wind speeds. However, the present study reveals that such a Doppler shift is observed as under the conditions of normal wind speeds. In this case, the weakly nonlinear approximation turns out to be applicable for describing the dispersion properties of not only small-amplitude waves but also nonlinear and even breaking waves. This implies that the intensive wave breaking at extreme high wind speeds occurs with the saturation (or dumping) of the wave height rather than the wavelength. This evidence might be helpful in investigating and modelling the wind-wave development at extreme high wind speeds.

4. Conclusion

The effects of the current on wind waves were investigated through laboratory experiments in three different wind-wave tanks ~~along~~ with a pump at Kyoto University, Japan, Kindai University, Japan, and IAP RAS. ~~In this experiment, 27 different types of currents were generated at wind speeds ranging from 7 to 67 m s^{-1}.~~ The study investigated 27 cases with carrying winds, waves, and currents, at wind speeds ranging from 7–67 m s^{-1}. We observed that the wind waves do not follow the dispersion relation in either the normal or the extremely high wind speeds in the three tanks (Fig. 4)—excluding case 25, in which the artificial current experiment used the Kindai tank. In case 25, U_{SURF} is approximately zero (Fig. 3); thus, the Doppler shift does not occur. Then, using 18 datasets (Kyoto and IAP RAS tanks) (Fig. 5), we found that the ratio of $C_S/C_{S,0}$ is constant at both normal and extremely high wind speeds. Moreover, in the artificial current experiment in Kindai, we observed that the ratio varies (Fig. 5). The evidence from the three tank experiments implies that the same wave-current interaction occurs at normal and extremely high wind speeds.

To develop an adequate model for wave-current interaction at normal and extremely high wind speeds, we validated four models (Figs. 6 and 7). At normal wind

speeds under 30 m s^{-1}, the wave frequency, wavelength, phase velocity of waves, and surface velocity of the water depended ~~were found to depend~~ on the wind speed (Fig. 3). However, the bulk velocity of the water showed a dependence on the tank type, i.e., ~~open tank~~ a large tank with a submerged wind-wave flume (IAP RAS) or ~~closed tank~~ wind flume above a tank (general type of wind-wave tank) (Kyoto University) (Fig. 3). The effect of the Doppler shift was confirmed at normal wind speeds, i.e., the significant waves were accelerated by the surface flow, and the phase velocity was represented as the sum of the surface velocity of water and the phase velocity, which is estimated by the dispersion relation of the deep-water waves (Fig. 6). At extreme high wind speeds over 30 m s^{-1}, a Doppler shift was observed similar to that under the conditions of normal wind speeds (Figs. 4 and 5). This suggests that the Doppler shift is an adequate model for representing the acceleration of wind waves by the current, not only for the wind waves at normal wind speeds but also for those with intensive breaking at extreme high wind speeds. The data obtained by the artificial current experiments conducted at Kindai University were used to explain how the artificial current accelerates (or decelerates) the significant waves. A weakly nonlinear model of surface waves at a shear flow was developed (Fig. 7). It was shown that it describes well the dispersion properties of not only small-amplitude waves but also strongly nonlinear and even breaking waves, typical for extreme wind conditions, with speeds, U_{10}, exceeding 30 m s^{-1}.

Acknowledgements

This work was supported by the Ministry of Education, Culture, Sports, Science and Technology (Grant-in-Aid No's. 18H01284, 18K03953, and 19KK0087). ~~This project was supported by the Japan Society for the Promotion of Science and the Russian Foundation for Basic Research under the Japan-Russia Research Cooperative Program.~~ This project was supported by the Japan Society for the Promotion of Science and the Russian Foundation for Basic Research (grant 18-55-50005) under the Japan-Russia Research Cooperative Program. We thank Prof. S. Komori and Mr. Tsuji for their help in conducting the experiments and for useful discussions. The experiments of IAP RAS were performed at the Unique Scientific Facility "Complex of Large-Scale Geophysical Facilities" (http://www.ckp-rf.ru/usu/77738/).

Appendix

It is important to estimate the phase velocity and wavelength of the significant

wind-waves using the water-level fluctuation data. Here, we explain the method, called as the cross-spectrum method. The water-level fluctuation $\eta(x, t)$ at arbitral location x and time t is shown as the equation:

$$\eta(x,t) = \int_{-\Omega}^{\Omega} A(\omega) e^{i(\omega t - k(\omega)x)} d\omega \quad \text{(A1)}$$

where ω is the angular frequency, $A(\omega)$ is the complex amplitude, and $k(\omega)$ is the wavenumber of waves having ω, Ω is the maximum angular frequency of the surface waves. $F_\eta(\omega)$ is the Fourier transformation of $\eta(x, t)$ when the measurement time t_m and Ω are sufficiently large. Using the inverse Fourier transformation of $F_\eta(\omega)$, $\eta(x, t)$ is shown as:

$$\eta(x,t) = \frac{1}{2\pi} \int_{-\Omega}^{\Omega} F_\eta(\omega) e^{i\omega t} d\omega. \quad \text{(A2)}$$

Comparing Eqs. (A1, A2), $F_\eta(\omega)$ is $F_\eta(\omega) = 2\pi A(\omega) e^{-ik(\omega)x}$. Assuming that the wind waves change the shape little between two wave probes set upstream and downstream, we can set the upstream and downstream water-level fluctuations $\eta_1(t) = \eta(0, t)$ and $\eta_2(t) = \eta(\Delta x, t)$, respectively, with Δx downstream from the first probe. The Fourier transformations $F_{\eta 1}(\omega)$ and $F_{\eta 2}(\omega)$ for $\eta_1(t)$ and $\eta_2(t)$, respectively, are shown as:

$$F_{\eta_1}(\omega) = 2\pi A(\omega), \quad \text{(A3)}$$

$$F_{\eta_2}(\omega) = 2\pi A(\omega) e^{-ik(\omega)\Delta x}. \quad \text{(A4)}$$

Then, the power spectra $S_{\eta 1 \eta 1}(\omega)$ and $S_{\eta 2 \eta 2}(\omega)$ for $\eta_1(t)$ and $\eta_2(t)$, respectively, are shown as:

$$S_{\eta_1\eta_1}(\omega) = \frac{1}{t_m} F^*_{\eta_1}(\omega) F_{\eta_1}(\omega) = \frac{1}{t_m} 4\pi^2 |A(\omega)|^2, \quad \text{(A5)}$$

$$S_{\eta_2\eta_2}(\omega) = \frac{1}{t_m} F^*_{\eta_2}(\omega) F_{\eta_2}(\omega) = S_{\eta_1\eta_1}(\omega). \quad \text{(A6)}$$

Here, the superscript * indicates the complex conjugate number. The cross-spectrum $Cr(\omega)$ for $\eta_1(t)$ and $\eta_2(t)$ is shown as:

$$Cr(\omega) = \frac{1}{t_m} F^*_{\eta 1}(\omega) F_{\eta 2}(\omega) = \frac{1}{t_m} 4\pi^2 |A(\omega)|^2 e^{ik(\omega)\Delta x}. \quad \text{(A7)}$$

Using Euler's theorem, Eq. (A7) transforms to:

$$Cr(\omega) = \frac{1}{t_m} 4\pi^2 |A(\omega)|^2 (\cos k(\omega)\Delta x + i \sin k(\omega)\Delta x)$$

$$= S_{\eta_1}(\omega)(\cos k(\omega)\Delta x + i \sin k(\omega)\Delta x). \quad \text{(A8)}$$

The cospectrum $Co(\omega)$ and quad spectrum $Q(\omega)$ are defined as the real and imaginary parts of $Cr(\omega)$, respectively, shown as $Cr(\omega) = Co(\omega) + iQ(\omega)$. Moreover, the phase $\theta(\omega)$

is defined as $\theta(\omega) = \tan^{-1}(Q(\omega)/ Co(\omega))$. Thus, $\theta(\omega)$ can be calculated as:

$$\theta(\omega) = \tan^{-1}(\tan(k(\omega)\Delta x) = k(\omega)\Delta x. \quad \text{(A9)}$$

Generally, the velocity of the wind waves C is defined as:

$$C = \frac{\omega}{k} = \frac{L}{T}, \quad \text{(A10)}$$

where L is the wavelength and T is the wave period. From Eqs. (A9, A10), $C(\omega)$ and $L(\omega)$ can be transformed to

$$C(\omega) = \frac{\omega}{k} = \frac{\omega\Delta x}{\theta(\omega)}, \quad \text{(A11)}$$

$$L(\omega) = \frac{2\pi}{k} = \frac{2\pi\Delta x}{\theta(\omega)}. \quad \text{(A12)}$$

When we estimate the phase $\theta_m(\omega_m)$ at the angular frequency of significant wind-waves ω_m ($=2\pi f_m$), the phase velocity of the significant wind waves C_S ($= C(\omega_m)$) and significant wavelength L_S ($= L(\omega_m)$) are calculated by:

$$C_S = \frac{2\pi f_m \Delta x}{\theta(f_m)}, \quad \text{(A13)}$$

$$L_S = \frac{2\pi\Delta x}{\theta(f_m)}. \quad \text{(A14)}$$

In the study, C_S and L_S are estimated by Eqs. (A13, A14) using the cross-spectrum method.

References

Dawe, J. T., Thompson, L., (2006), Effect of ocean surface currents on wind stress, heat flux, and wind power input to the ocean, Geophysical Research Letters, 33, L09604, doi:10.1029/2006GL025784

Donelan, M.A., Haus, B.K., Reul, N., Plant, W.J., Stiassnie, M., Graber, H.C., Brown, O.B., Saltzman, E.S., (2004), On the limiting aerodynamic roughness of the ocean in very strong winds, Geophysical Research Letters, 31, doi:10.1029/2004GL019460. L18306

Fan, Y., Ginis, I., Hara, T., (2009), The Effect of Wind–Wave–Current Interaction on Air–Sea Momentum Fluxes and Ocean Response in Tropical Cyclones, Journal of Physical Oceanography, 39, pp. 1019-1034.

505 Iwano, K., Takagaki, N., Kurose, R., Komori, S., (2013), Mass transfer velocity across
506 the breaking air-water interface at extremely high wind speeds, Tellus B 65, 21341,
507 doi:10.3402/tellusb.v65i0.21341
508 Kara, A. B., Metzger, E. J., Bourassa, M. A., (2007), Ocean current and wave effects on
509 wind stress drag coefficient over the global ocean, Geophysical Research Letters,
510 34, L01604, doi:10.1029/2006GL027849
511 Kawabe, M., (1988), Variability of Kuroshio velocity assessed from the sea-level
512 difference between Naze and Nishinoomote, Journal of oceanographical Society of
513 Japan, 44, pp. 293-304.
514 Kelly, K. A., Dickinson, S., McPhaden, M. J., Johnson, G. C., (2001), Ocean currents
515 evident in satellite wind data, Geophysical Research Letters, 28(12), pp.
516 2469-2472.
517 Komori, S., Iwano, K., Takagaki, N., Onishi, R., Kurose, R., Takahashi, K., Suzuki, N.,
518 (2018), Laboratory measurements of heat transfer and drag coefficients at
519 extremely high wind speeds, Journal of Physical Oceanography,
520 doi:10.1175/JPO-D-17-0243.1
521 Krall, K. E., Jähne, B., (2014), First laboratory study of air-sea gas exchange at hurricane
522 wind speeds, Ocean Science, 10(2), 257-265, doi:10.5194/os-10-257-2014
523 Krall, K. E., Smith, A. W., Takagaki, N., Jähne, B., (2019), Air–sea gas exchange at wind
524 speeds up to 85 m s-1, Ocean Science, 15(6), doi: 10.5194/os-15-1783-2019
525 Powell, M. D., Vickery, P. J., Reinhold, T. A., (2003), Reduced drag coefficient for high
526 wind speeds in tropical cyclones, Nature, 422, 279–283, doi:10.1038/nature01481
527 Shi, Q., Bourassa, M. A., (2019), Coupling Ocean Currents and Waves with Wind Stress
528 over the Gulf Stream, Remote Sensing, 11, 1476, doi:10.3390/rs11121476
529 Simmen, J. A., Saffman, P. G., (1985), Steady deep-water waves on a linear shear current,
530 Studies in Applied Mathematics, 73, 35–57, doi: 10.1002/sapm198573135
531 Takagaki, N., Komori, S., Suzuki, N., Iwano, K., Kuramoto, T., Shimada, S., Kurose, R.,
532 Takahashi, K., (2012), Strong correlation between the drag coefficient and the
533 shape of the wind sea spectrum over a broad range of wind speeds, Geophysical
534 Research Letters, 39, doi:10.1029/2012GL053988. L23604
535 Takagaki, N., Komori, S., Suzuki, N., Iwano, K., Kurose, R., (2016), Mechanism of drag
536 coefficient saturation at strong wind speeds, Geophysical Research Letters, 43,
537 doi:10.1002/2016GL070666
538 Takagaki, N., Komori, S., Ishida, M., Iwano, K., Kurose, R., Suzuki, N., (2017),
539 Loop-type wave-generation method for generating wind waves under long-fetch

conditions, Journal of Atmospheric Oceanic Technology, 34(10), 2129–2139, doi:10.1175/JTECH-D-17-0043.1

Takagaki, N., Suzuki, N., Takahata, S., Kumamaru, H., (2020), Effects of air-side freestream turbulence on development of wind waves, Experiments in Fluids, 61, 136, doi:10.1007/s00348-020-02977-9

Troitskaya, Y. I., Sergeev, D. A., Kandaurov, A. A., Baidakov, G. A., Vdovin, M. A., Kazakov, V. I., (2012), Laboratory and theoretical modeling of air-sea momentum transfer under severe wind conditions, Journal of Geophysical Research, 117, C00J21, doi:10.1029/2011JC007778

Troitskaya, Y., Sergeev, D., Vdovin, M., Kandaurov, A., Ermakova, O., Takagaki, N., (2020), Laboratory study of the effect of surface waves on heat and momentum transfer at strong winds, Journal of Geophysical Research Oceans, doi: 10.1029/2020JC016276